High Interfacial Shear Strength and High Tensile Strength in Heterocyclic Aramid Fibers with Improved Interchain Interaction

Jiajun Luo, Yeye Wen, Tao Li, Xiangzheng Jia, Xudong Lei, Ziyi Zhang, Zhihua Xiao, Xianqian Wu, Zhenfei Gao, Enlai Gao, Kun Jiao,* and Jin Zhang*

As a typical kind of high-performance fibers, heterocyclic aramid fibers are widely used to reinforce resins to prepare advanced lightweight composites with high mechanical performances. However, their poor interfacial shear strength limits the combination with resins and leads to undesirable interfacial strength of composites. Thus, heterocyclic aramid fibers with high interfacial shear strength and high tensile strength are highly desired. Herein, heterocyclic aramid fibers with a high interfacial shear strength of 40.04 ± 2.41 MPa and a high tensile strength of 5.08 ± 0.24 GPa are reported, in which the nitrile-modified poly-(benzimidazole-terephthalamide) polymer chains are crosslinked by azide-functionalized graphene oxide nanosheets. The improved interchain interaction can conquer the splitting of nanofibrils and strengthen the skin-core layer of heterocyclic aramid fibers, while the graphene oxide can induce an ordered arrangement of polymer chains to improve the crystallinity and orientation degree of fibers. These two effects account for the high interfacial shear strength and high tensile strength of heterocyclic aramid fibers. These findings have provided a strategy to efficiently enhance the interfacial shear strength as well as the tensile strength of high-performance fibers.

1. Introduction

As a kind of high-performance fiber, aramid fibers with light weight and excellent mechanical performances have been widely developed.[1–4] Various types of aramid fibers have been industrialized, including Kevlar and Nomex from DuPont, Twaron and Technora from Teijin, Heracron from Kolon, and so on.[5,6] However, due to the strong hydrogen bonds between the aramid polymer chains, a strong acid solvent is required to dissolve the aramid polymer before spinning, leading to a dangerous processing procedure and environmental pollution.[7–9] Even so, it is difficult to realize the high orientation of polymer chains in the spinning process. Therefore, the mechanical properties of those fibers are restricted (below 4.5 GPa). Heterocyclic aramid fibers (HAFs) are modified aramid fibers, containing aromatic rings and heterocyclic rings in the polymer chain.[10] The existence of a heterocyclic structure can realize the direct spinning of polymer solution with a high draw ratio, resulting in the high crystallinity and high orientation degree of fibers.[11] HAFs featuring excellent mechanical performances, are vital materials in aeronautical engineering, special protection equipment, and civil field, and have also been industrialized in global corporations, including Kolon, Zhonglan Chenguang Chemical Research Institute, DuPont, Kamensk, and so on, which provides a broader perspective on the industry landscape.[12–15]

Considering their applications in extreme tension-dominated fields, the fabrication of HAFs with ultrahigh tensile properties

J. Luo, Y. Wen, Z. Zhang, Z. Xiao, K. Jiao, J. Zhang
Beijing National Laboratory for Molecular Sciences
School of Materials Science and Engineering
College of Chemistry and Molecular Engineering
Academy for Advanced Interdisciplinary Studies
Beijing Science and Engineering Center for Nanocarbons
Peking University
Beijing 100871, China
E-mail: jiaokun-cnc@pku.edu.cn; jinzhang@pku.edu.cn

J. Luo, Y. Wen, T. Li, Z. Xiao, Z. Gao, K. Jiao, J. Zhang
Beijing Graphene Institute (BGI)
Beijing 100095, China

Y. Wen
Advanced Research Institute of Multidisciplinary Science
Beijing Institute of Technology
Beijing 100081, China

X. Jia, E. Gao
Department of Engineering Mechanics
School of Civil Engineering
Wuhan University
Wuhan 430072, China

X. Lei, X. Wu
Institute of Mechanics
Chinese Academy of Sciences
Beijing 100190, China

X. Lei, X. Wu
School of Engineering Science
University of Chinese Academy of Sciences
Beijing 100049, China

has been constantly pursued.[6,16,17] Notably, the application in various fields of HAFs often requires their combination with matrix materials, for example, epoxy resin, to fabricate HAFs reinforced composite materials.[18,19] The failure mechanism of composite materials mainly includes fiber fracture and debonding between fiber and resin.[20,21] To obtain high-performance composites, the tensile strength of fibers and the bond strength between fibers and resins need to be considered. The interfacial shear strength (IFSS) is an important index to evaluate the bond strength between fiber and resin. Therefore, it is of great practical importance to prepare HAFs with high tensile strength and high IFSS.[22] HAFs possess a high degree of orientation and crystallinity, and good alignment of polymer chains along the axial direction, which endow them with high tensile strength.[6,23–25] However, the only weak lateral interaction based on interchain N—H—O hydrogen bonding can lead to the splitting of nanofibrils in HAFs under shear stress.[26–28] The heterogeneity of HAF chains between skin and core resulting from the wet spinning process prevents the further extension of shear stress from the skin part to the core part.[29–33] Moreover, the inert and smooth surface of HAFs makes it difficult to form strong bonds with matrix materials.[34] These factors result in a low IFSS of HAFs, limiting their practical applications.

Focusing on structural optimization to improve the IFSS of HAFs, a lot of methods referring to the cross-linking of polymer chains and surface modification of aramid fibers have been developed.[35–45] Surface modification usually includes physical and chemical approaches, such as high-energy radiation treatment,[36–38] surface coating,[39–40] chemical grafting,[41–44] and acid-base corrosion.[45] However, these strategies usually have adverse effects on the tensile strength. For example, the crosslink of polymer chains can help overcome the splitting of nanofibrils and the adverse effect of the skin-core structure by increasing the lateral interaction, but simultaneously reducing the degree of orientation and crystallinity of HAFs by disturbing the alignment of the polymer chain.[42] Surface treatment of HAFs by chemical and physical methods, such as chemical grafting, surface coating, plasma irradiation, and so on, can improve surface polarity and roughness to enhance their combination with a matrix.[34,43–45] However, these strategies not only lead to a decrease in tensile strength by destroying the dense structure of fibers, but also require complicated steps. Therefore, it is crucial to develop a simple method to attain both high IFSS and high tensile strength in HAFs.

The introduction of nanomaterials into polymers to obtain high mechanical properties has aroused great interest among researchers.[46–51] Carbon nanotubes, graphene, and their derivates are typical nano additives for their induction effects on the crystallization and orientation of polymer chains.[48,52,53] Among them, due to the lack of functional groups, carbon nanotubes, and graphene have weak interactions with polymer chains and are difficult to disperse in polymer matrixes. These two effects can cause restricted mechanical performances of composites reinforced by carbon nanotubes and graphene. GO, a derivative of graphene, has many functional groups on the nanosheet, such as epoxy, hydroxy, and carboxy groups.[54] It has good dispersity and offers a platform to efficiently engineer its interactions with polymer chains via chemical bonding, electrostatic interactions, π-π interactions, and so on.[55,56] In addition,

the effect of GO on the microstructure of polymers is also prominent. It has been proved that GO can induce the crystallization and orientation of polymer chains.[57] Therefore, GO provides an opportunity to simultaneously improve the interchain interaction and optimize the microstructure of the polymer.

Herein, we introduced a new monomer 2-nitrile-p-phenylenediamine (PPD-CN) containing reactive nitrile functional groups as the fourth monomer to participate in the copolymerization of heterocyclic aramid poly(p-phenylene-benzimidazole-terephthalamide) (PBIA) monomers [p-phenylenediamine (PPD), 2-(4-aminophenyl)−5-aminobenzimidazole (PABZ), and terephthaloyl chloride (TPC)]. Azide-functionalized GO (GO-N_3) was added in situ to prepare composite spinning dopes. The composite fibers (GO-N_3/PBIA-CN) were prepared via the wet spinning and heat treatment process. Compared to PBIA fibers, the introduction of PPD-CN increases the polarity of the PBIA chain and provides active sites for crosslinking, but disrupts the chain regularity and decreases the degree of orientation and crystallinity of modified PBIA (PBIA-CN) fibers. However, the addition of GO-N_3 can induce the orientation and crystallinity of polymer chains, which repair the structural destruction induced by PPD-CN. Importantly, GO-N_3 can improve the interchain interactions by undergoing a "click" reaction with PBIA-CN chains upon heat treatment, to prevent the splitting of nanofibrils and destruction of the skin-core layer (**Figure 1**a; Figure S1, Supporting Information). As a result, the composite GO-N_3/PBIA-CN fibers with a high interfacial shear strength (IFSS) of 40.04 MPa and a high tensile strength of 5.08 GPa (Figure 1b,c; Figure S2, Supporting Information) were prepared by a design of heterocyclic aramid chains. Moreover, GO-N_3/PBIA-CN fibers possess a dynamic IFSS (DIFSS) as high as 66.79 MPa at a strain rate of 1400 s^{-1} and superior impregnated properties, indicating their potential applications in impact protective composites (Figure 1c).

2. Results and Discussion

2.1. Structural Design and Characterization of GO-N_3

The graphite powder (8000 mesh) was used as a raw material to prepare GO with an average sheet size of 1.4 µm (**Figure 2**a). After oxidation of the graphite powder, GO nanosheets contain a lot of carboxyl groups, which can be used as reactive sites to prepare GO-N_3 (Figure 2b). Compared to GO, the signal peaks of N 1s can be observed in X-ray photoelectron spectroscopy (XPS) of GO-N_3 (Figure S3, Supporting Information). The successful modification of azide functional groups on GO sheets can be further demonstrated by XPS spectra of C 1s and N 1s of GO-N_3 (Figure 2c,d). From means of XPS-peak-differentiation-imitating analysis of C 1s of GO-N_3, five C signal peaks can be obtained [C=C ($\approx$284.8 eV), C—C ($\approx$285.5 eV), C—O/C—N (286.7 eV), C=O (287.6 eV), and HO—C=O ($\approx$289.0 eV)].[58] Particularly, compared to GO, the HO—C=O content of GO-N_3 was reduced. The XPS spectrum of N 1s of GO-N_3 reflects the presence of functional groups of N=N=N and NH—C=O. In addition, the ratio of contents ascribed to the N element of N=N=N to that of N=N=N is close to 2. The absorption peak at $\approx$2100 cm^{-1} derived from the stretching vibration of the azide functional groups can be observed in the FTIF spectroscopy of GO-N_3, which is absent in the
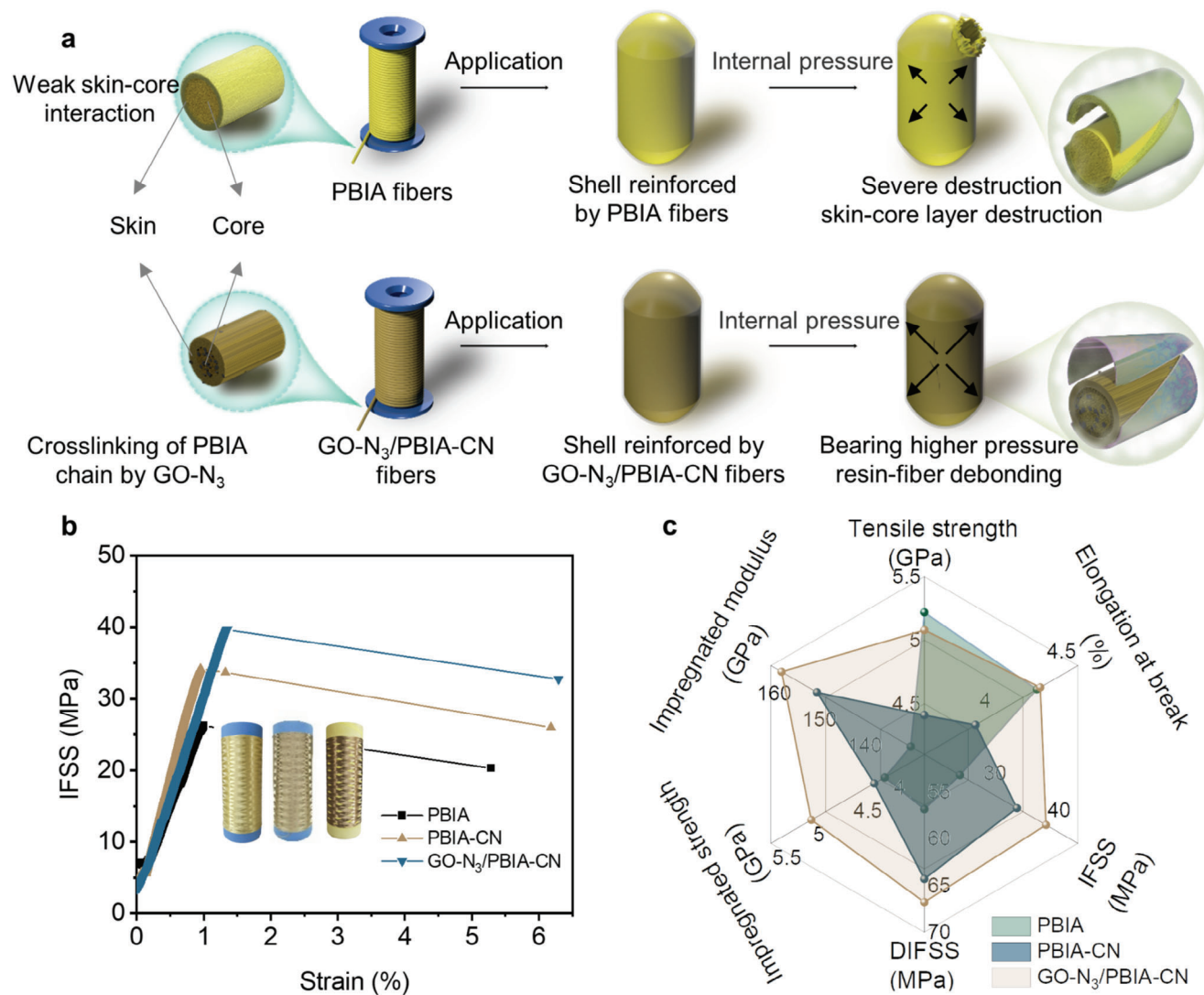
Figure 1. a) Schematic diagram of the microstructure and potential applications of PBIA and GO-N_3/PBIA-CN fibers. The cross-linking of PBIA-CN chains by GO-N_3 can prevent the destruction of the skin-core layer of GO-N3/PBIA-CN fibers, thereby bearing greater loads and preventing material failure. b) IFSS-versus-strain curves of different fibers for IFSS tests. c) A radial plot comparing the mechanical properties of different fibers.

FTIF spectroscopy of GO (Figure 2e). The result jointly confirms the successful preparation of GO-N_3.

2.2. Preparation and Structural Characterization of GO-N_3/PBIA-CN

The as-prepared GO-N_3 was in situ added into the polymerization system containing four monomers (PPD, PABZ, PPD-CN, and TPC) to prepare spinning dope of GO-N_3/PBIA-CN. After the wet spinning and heat treatment process, GO-N_3/PBIA-CN fibers were prepared (Figure S4, Supporting Information). Subsequently, all fibers were prepared by the same optimal process parameters as GO-N_3/PBIA-CN fibers. To be specific, the concentration of GO-N_3 to the polymer is optimal at 0.05 wt.% in GO-N_3/PBIA and GO-N_3/PBIA-CN fibers, and the molar ratio of PPD to PPD-CN is 2:1 in PBIA-CN and GO-N_3/PBIA-CN fibers

if there is no further description. Compared to PBIA fibers, the FTIF spectroscopy of PBIA-CN and GO-N_3/PBIA-CN fibers exhibit an infrared absorption peak of the nitrile functional group at ≈2250 cm^{-1}, demonstrating the successful introduction of the nitrile functional group on PBIA chains (Figure S5, Supporting Information). During the heat treatment process (390 °C), the reaction between azide functional groups in GO-N_3 and nitrile groups in PBIA-CN chains occurred, forming tetrazole rings (Figure 1a; Figure S1, Supporting Information). Since the concentration of GO-N_3 in fibers is as low as 0.05 wt.%, the signal of tetrazole rings in samples is difficult to observe. NEXAFS spectra of fibers were collected to verify the crosslinking of PBIA-CN chains by GO-N_3 (Figure 2f). Compared to PBIA fibers, PBIA-CN fibers have an obvious peak of Ar-CN (285.5 eV). Although this characterization technique possesses high resolution, the overlapped absorbance peaks of the tetrazole ring (401.3 eV) and heterocyclic monomer in polymer chains (401.3 eV) in the spectrum of
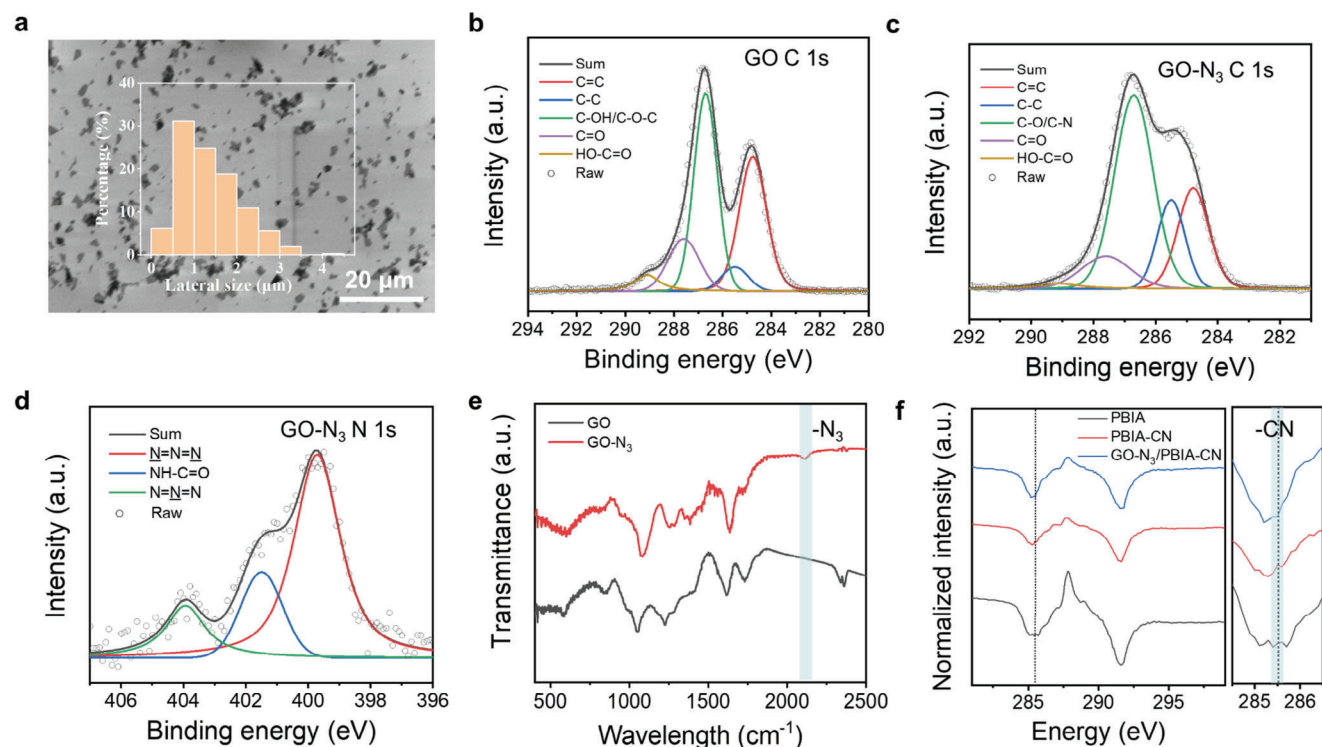
ADVANCED
SCIENCE NEWS
www.advancedsciencenews.com

ADVANCED
FUNCTIONAL
MATERIALS
www.afm-journal.de

Figure 2. a) Scanning electron microscope (SEM) image of GO sheets, the inset shows the statistical graph of the lateral size of GO nanosheets. XPS spectrum of b) C 1s of GO, c) C 1s of GO-N$_3$, d) N 1s of GO-N$_3$. e) FTIR spectroscopy of GO and GO-N$_3$. f) NEXAFS spectra of PBIA, PBIA-CN, and GO-N$_3$/PBIA-CN fibers, the spectrum on the right side is an enlarged area of the spectrum on the left side.

GO-N$_3$/PBIA-CN make it difficult to directly verify the crosslinking sites. However, the peak of Ar-CN in the spectrum of GO-N$_3$/PBIA-CN disappears compared to that of PBIA-CN fibers, which may be attributed to the reaction between nitrile groups in PBIA-CN chains and azide functional groups in GO-N$_3$.[59] This result can help verify the crosslinking of PBIA-CN chains by GO-N$_3$.

Due to the same spinning process, the surface morphologies and diameter (≈16 μm) of PBIA, GO-N$_3$/PBIA, PBIA-CN, and GO-N$_3$/PBIA-CN observed from SEM images are similar (**Figure 3**a,b; Figures S6 and S7, Supporting Information). In addition, Fibers containing different ratios of PPD to PPD-CN also possess similar surface morphologies, which further proves that the introduction of GO-N$_3$ and PPD-CN does not affect the preparation of fibers. The transmission electron microscope (TEM) images of the axial cross-section of the GO-N$_3$/PBIA-CN fiber show that GO-N$_3$ is well dispersed inside the fiber (Figure 3c,d).

The misorientation angle of microfibers derived from the patterns of small-angle X-ray scattering (SAXS) can be used to probe the orientation of the microstructure of fibers (Figure 3e–h). The results demonstrate that the addition of GO-N$_3$ contributes to a significant decrease in the misorientation angle in GO-N$_3$/PBIA fibers and GO-N$_3$/PBIA-CN fibers (from 5.08 for PBIA to 3.41 for GO-N$_3$/PBIA and from 6.86 for PBIA-CN to 4.85 for GO-N$_3$/PBIA-CN), indicating that GO-N$_3$ can induce the arrangement of microfibers (Figure 3m). Wide-angle X-ray scattering (WAXS) patterns of fibers were collected to evaluate the crystallinity and orientation of fibers (Figure 3i–l). The results

demonstrate that the addition of GO-N$_3$ contributes to a significant decrease in the full width at half maxima of radial integration curves in the equatorial of the WAXS patterns (from 2.26 for PBIA to 1.53 for GO-N$_3$/PBIA and from 3.32 for PBIA-CN to 2.44 for GO-N$_3$/PBIA-CN), indicating that the crystallinity of GO-N$_3$/PBIA and GO-N$_3$/PBIA-CN fibers are greatly improved compared with PBIA and PBIA-CN fibers, respectively (Figure 3n; Figure S8a, Supporting Information). By integrating the curve against the azimuthal degree of WAXS patterns, the calculated crystalline orientation degree of GO-N$_3$/PBIA (0.931) and GO-N$_3$/PBIA-CN (0.923) fibers are higher than that of PBIA (0.920) and PBIA-CN (0.916) fibers, respectively, indicating that the orientation degree of fibers is improved by addition of GO-N$_3$ (Figure 3m; Figure S8b, Supporting Information). It is worth noting that the introduction of nitrile groups to the PBIA chain has an adverse effect on the microstructures of PBIA-CN fibers since they disrupt the regularity of PBIA chains (Figure 3m,n). The more nitrile groups are introduced, the more severe the effect becomes (Figures S9 and S10, Supporting Information). However, the addition of GO-N$_3$ can help induce the orientation and crystalline of PBIA-CN chains to significantly optimize the microstructures of composite PBIA-CN fibers. The structures of GO-N$_3$/PBIA-CN fibers with different concentrations of GO-N$_3$ were probed. The result shows that too much addition of GO-N$_3$ can decrease the crystallinity of GO-N$_3$/PBIA-CN, which might originate from the aggregation of GO-N$_3$ (Figure S11, Supporting Information). The optimized concentration of GO-N$_3$ was determined as 0.05 wt.%. In addition, the thermogravimetric curves show that GO-N$_3$/PBIA-CN fibers have higher mass

ADVANCED
SCIENCE NEWS

www.advancedsciencenews.com

ADVANCED
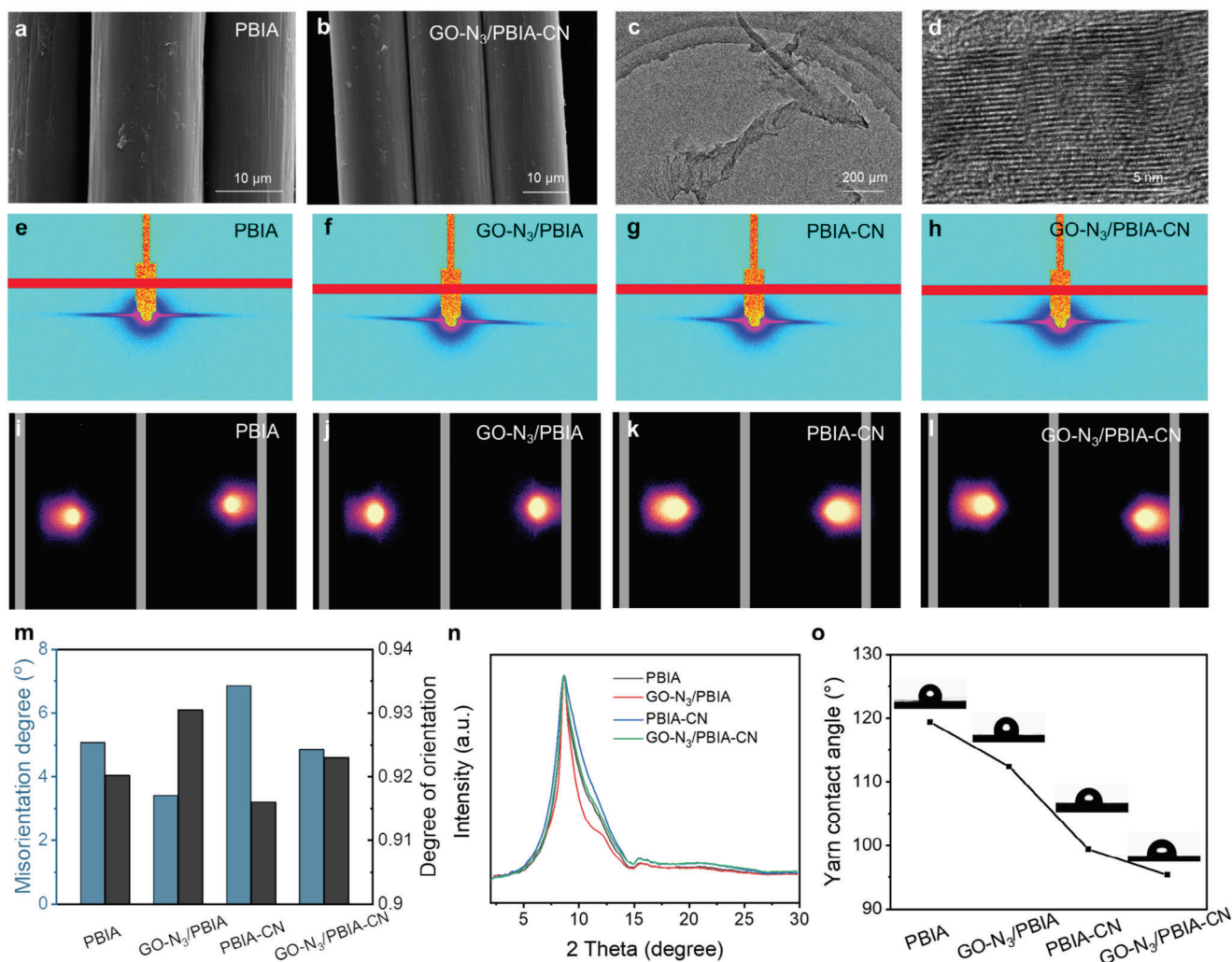**FUNCTIONAL**
MATERIALS

www.afm-journal.de

Figure 3. SEM images of a) PBIA and b) GO-N$_3$/PBIA-CN fibers. c) TEM image and d) High-resolution TEM image of the axial cross-section of the GO-N$_3$/PBIA-CN fiber. 2D-SAXS patterns of composite fibers: e) PBIA, f) GO-N$_3$/PBIA, g) PBIA-CN, and h) GO-N$_3$/PBIA-CN fibers. 2D-WAXS patterns of composite fibers: i) PBIA, j) GO-N$_3$/PBIA, k) PBIA-CN, and l) GO-N$_3$/PBIA-CN fibers. m) Comparison of the misorientation angle and degree of orientation of different fibers derived from 2D-SAXS and 2D-WAXS analysis, respectively. n) 1D-WAXS curves of different fibers derived from 2D-WAXS analysis. o) Comparison of the contact angle of different fibers, the inserts show the corresponding digital photographs.

retention than PBIA-CN, indicating the better thermal stability of GO-N$_3$/PBIA-CN fibers, which originates from their high crystallinity and high orientation degree (Figure S12, Supporting Information).

The contact angle and surface energy of fiber yarns as well as the surface roughness of the single fiber are used to evaluate the surface polarity and roughness. The addition of GO-N$_3$ and PPD-CN can decrease the contact angle and increase the surface energy of fiber yarns (Figure 3o; Figures S13 and S14, Supporting Information). GO-N$_3$/PBIA-CN fibers have the smallest contact angle and the largest surface energy, indicating that the GO-N$_3$/PBIA-CN process has the greatest polarity, which can improve their binding energy with the matrix materials. Moreover, GO-N$_3$/PBIA-CN fibers show the highest surface roughness. The result implies that they have the largest contact area with matrix materials, which is in favor of a good interface combination (Figures S15–S19, Supporting Information).

2.3. Mechanical Performances of GO-N$_3$/PBIA-CN

The uniaxial tensile tests and the single fiber pull-out experiment can be used to test the tensile performances and IFSS, respectively (Figure S20, Supporting Information). The optimal amount of GO-N$_3$ addition (0.05 wt.%) can achieve the highest tensile strength of GO-N$_3$/PBIA-CN (Figure S21, Supporting Information). GO-N$_3$/PBIA-CN fibers with other concentrations of GO-N$_3$ show inferior performances due to low crystallinity and orientation degree resulting from an inadequate addition or aggregation of GO-N$_3$. The PBIA fibers exhibit a tensile of 5.22 ± 0.42 GPa and an elongation at break of $4.26 \pm 0.50\%$, whereas their IFSS is only 26.57 ± 2.18 MPa (**Figure 4**a,b). The IFSS of PBIA-CN fibers is increased to 35.49 ± 3.21 MPa due to the introduction of polar nitrile functional groups, but the decreasing of crystallinity and orientation degree in PBIA-CN fibers results in a low tensile strength of only 4.41 ± 0.10 GPa, which

**ADVANCED
SCIENCE NEWS**

www.advancedsciencenews.com
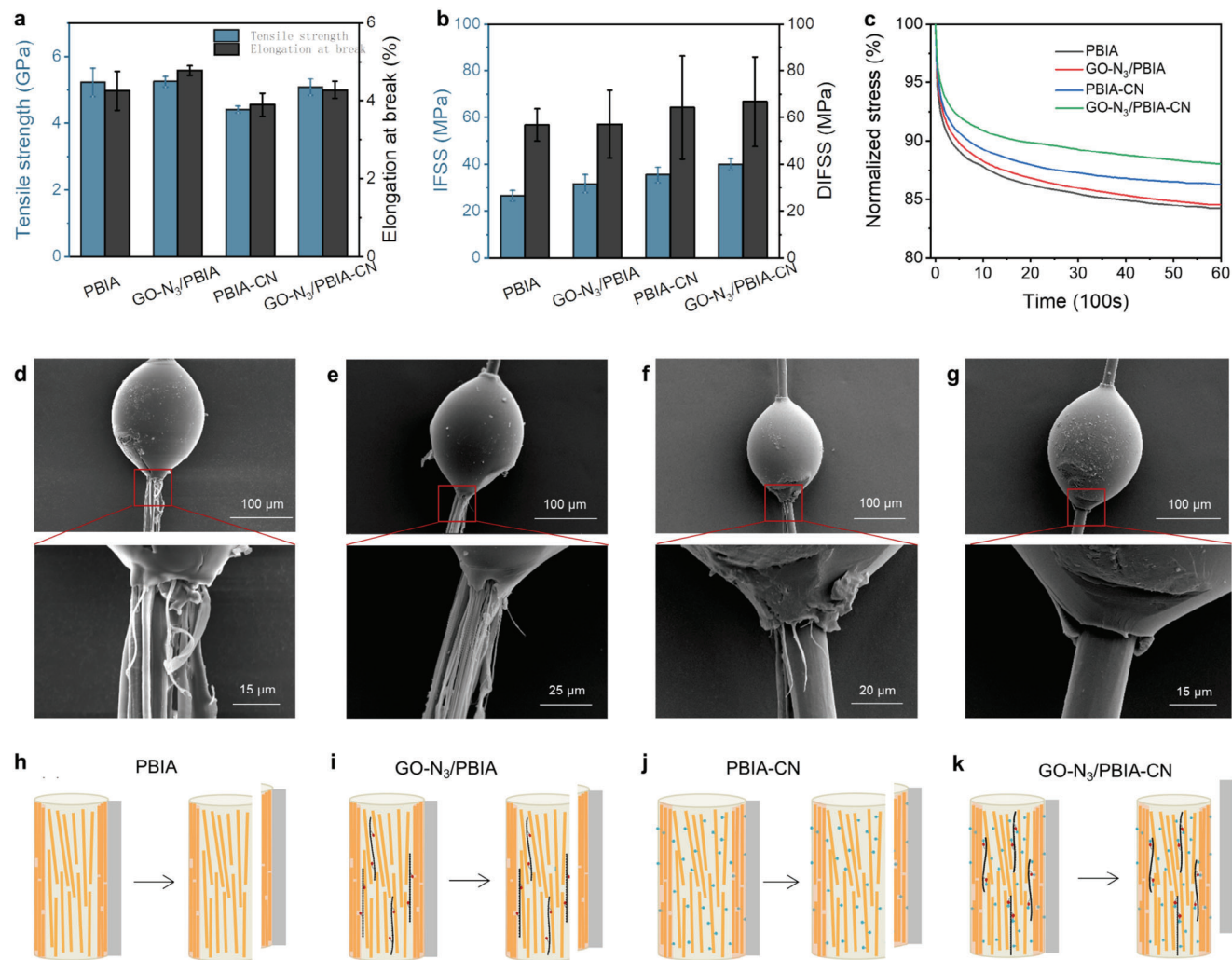
**ADVANCED
FUNCTIONAL
MATERIALS**

www.afm-journal.de

Figure 4. a) Comparison of the tensile strength and elongation at the break of different fibers. b) Comparison of the IFSS and DIFSS of different fibers. c) Stress relaxation curves of different fibers at 1.5% strain. SEM images of the d) PBIA, e) GO-N$_3$/PBIA, f) PBIA-CN, and g) GO-N$_3$/PBIA-CN fiber after micro-drop embedding and single fiber pull-out experiment. Schematic diagram of interfacial failure behavior of h) PBIA, i) GO-N$_3$/PBIA, g) PBIA-CN, and k) GO-N$_3$/PBIA-CN fibers.

is 15.5% lower than that of PBIA fibers. Although the introduction of polar functional groups is beneficial to the improvement of interfacial properties, it significantly sacrifices the tensile performance of fibers. This conclusion is also similar to the result of the reported work using monomers containing chlorine functional groups to modify HAFs.[13] However, the tensile strength of GO-N$_3$/PBIA-CN fibers can be improved to 5.08 ± 0.24 GPa because of the improved degree of crystallinity and orientation by compositing GO-N$_3$, which shows only a 3% decrease compared to PBIA fibers. The IFSS of GO-N$_3$/PBIA-CN (40.04 ± 2.41 MPa) is significantly enhanced by 50% compared to PBIA fibers. Therefore, GO-N$_3$/PBIA-CN fibers show excellent mechanical performances (Figure 4a,b; Figures S22 and S23, Supporting Information). In addition, compared to PBIA fibers, small improvements were observed in the tensile properties and IFSS of GO-N$_3$/PBIA fibers. In addition, compared to commercial Kevlar 129 and carbon fiber T700 fibers, GO-N$_3$/PBIA-CN fibers have significant

advantages in tensile strength and elongation at break (Figure S24, Supporting Information).[5,60]

Understanding the interfacial behaviors of fibers under various loading rates can help to evaluate the performance of fibers under practical impact situations. Therefore, the single fiber pull-out experiment with different loading rates was performed (Figure S25, Supporting Information). The results show that all fibers exhibit a distinct strain-rate interfacial strengthening effect (Figure 4b). With the increase of the strain rate, the dynamic IFSS (DIFSS) of all fibers becomes higher. Especially, the DIFSS of GO-N$_3$/PBIA-CNs is as high as 66.79 ± 19.13 MPa at a strain rate of 1400 s^{-1}, which is much higher than those of PBIA fibers (56.85 ± 6.94 MPa), GO-N$_3$/PBIA fibers (57.17 ± 14.52 MPa), and PBIA-CN fibers (64.31 ± 22.103 MPa), indicating the stronger interaction between GO-N$_3$/PBIA-CN fibers and resins at a high strain rate under practical impact situations.

**ADVANCED
SCIENCE NEWS**

www.advancedsciencenews.com

**ADVANCED
FUNCTIONAL
MATERIALS**

www.afm-journal.de

2.4. Mechanism Discussion on the Mechanical Performances of GO-N$_3$/PBIA-CN

The high tensile strength of GO-N$_3$/PBIA fibers is mainly attributed to the improved degree of orientation and crystallinity of PBIA-CN fibers under the inductive effect of GO-N$_3$, which is consistent with the previous works.[13] In addition, stress relaxation curves show that the initial stress retention of GO-N$_3$/PBIA-CN fibers (88.04%) is higher than those of PBIA-CN (86.29%), GO-N$_3$/PBIA (84.54%), and PBIA (84.23%) fibers (Figure 4c). The higher resistance to the interchain slippage of GO-N$_3$/PBIA-CN fibers originated from the strong interaction based on covalent bonding between GO-N$_3$ and PBIA-CN chains, which can promote stress transfer and suppress strain localization. As a result, the crosslinking effect of GO-N$_3$ is also beneficial for the improvement of tensile properties.[12]

As for the IFSS, it is commonly related to the surface properties of fibers. Although the surface polarity of PBIA-CN and GO-N$_3$/PBIA-CN fibers was improved compared to that of PBIA fibers, the magnitude of the improvement is insufficient to explain the IFSS increased effect up to 50%. To further analyze the underlying mechanism of the improvement, we observed the morphology of fibers and resin microdroplets after the single fiber pull-out experiment (Figure 4d–g). Splitting of fibers was observed along the axial direction of PBIA, GO-N$_3$/PBIA, and PBIA-CN fibers, so their interfacial failure mechanism is mainly because of the splitting of nanofibrils and destruction of the skin-core structure (Figure 4h–j). However, the surface structure of GO-N$_3$/PBIA-CN fibers was kept intact after the pull-out experiment, implying that the interfacial failure mechanism of GO-N$_3$/PBIA-CN fibers is based on the separation of resin-fiber interfaces (Figure 4k).

To further explore the different interfacial failure mechanisms between GO-N$_3$/PBIA-CN and other fibers, we did atomistic simulations and relevant analyses (Figures S26 and S27, Supporting Information). The binding energy between GO and PBIA-CN chains (50.88 meV per atom) is higher than that between PBIA-CN chains and resin (29.23 meV per atom). Therefore, for the composite in which GO-N$_3$/PBIA-CN fibers are embedded in a micro-drop of resin, the skin-core layer of the GO-N$_3$/PBIA-CN fiber is stronger than the fiber-resin interface, which leads to the separation of fiber-resin interface under a shear force. However, the binding energies between PBIA chains in PBIA fibers (27.48 meV per atom) and between PBIA-CN chains in PBIA-CN fibers (26.31 meV per atom) are smaller than those between their corresponding polymer chains and resins (29.01 and 29.23 meV per atom, respectively), leading to the destruction of the skin-core structure of fibers. Therefore, the design of the covalent bonding between GO-N$_3$ and PPD-CN chains in GO-N$_3$/PBIA-CN fibers can change the interfacial failure mode from skin-core destruction to resin-fiber debonding, which accounts for the improvement of IFSS.

The effect of the nitrile functional groups is further analyzed by tailoring the content of PPD-CN in fibers (Figures S28 and S29, Supporting Information). When the molar ratio of PPD to PPD-CN is 1:1, the corresponding GO-N$_3$/PBIA-CN fibers exhibit a tensile strength of only 4.77 ± 0.35 GPa and an IFSS of 34.29 ± 3.13 MPa which is both smaller than those of composite fibers in which molar ratio of PPD to PPD-CN is 2:1. For

GO-N$_3$/PBIA-CN fibers with higher molar ratio of PPD to PPD-CN (3:1), they also exhibit inferior mechanical performances (4.75 ± 0.36 GPa in tensile strength and 36.33 ± 2.14 MPa in IFSS). Higher content of nitrile functional groups in PBIA-CN chain bring more adverse effect on the microstructure of PBIA-CN fibers, making the microstructure of fiber looser, which is beyond the induction effect of optimized addition of GO-N$_3$ (Figures S7 and S8, Supporting Information). Lower content of nitrile functional groups may reduce the active sites of PBIA-CN chains to crosslink with GO-N$_3$, thus restricting the improvement of tensile properties and IFSS by GO-N$_3$ addition. However, at either higher or lower contents of PPD-CN, the addition of GO-N$_3$ can help conquer the destruction of skin-core structure and significantly increase the IFSS of composite fibers (Figure S30, Supporting Information), which further demonstrates that the IFSS properties of HAFs are dominated by the lateral interaction of fibers, and it is effective to improve the interfacial properties by enhancing the interchain interaction.

2.5. Impregnated Performances of GO-N$_3$/PBIA-CN

To further demonstrate the advantage of GO-N$_3$/PBIA-CN fibers with high tensile strength in combination with high IFSS, we prepared the impregnated fibers and explored their mechanical properties (**Figure 5**a). The impregnated GO-N$_3$/PBIA-CN fibers exhibit the highest mechanical properties, showing a tensile strength of 5.00 ± 0.19 GPa and a modulus of 162.6 ± 3.28 GPa (Figure 5b,c). Compared to the mechanical properties of impregnated PBIA fibers, the tensile strength and modulus of GO-N$_3$/PBIA-CN fibers are improved by 22.2% and 21.3%, respectively, indicating their application potential as structural reinforced fibrous materials. According to SEM images of impregnated fibers after the tensile test, the cross-section of impregnated GO-N$_3$/PBIA-CN fibers after destruction is neat and shows few fibrillations, while those of impregnated PBIA, GO-N$_3$/PBIA, and PBIA-CN fibers are seriously damaged (Figure 5d–g). The result indicates that GO-N$_3$/PBIA-CN fibers have strong lateral interaction and strong binding force with resin. Therefore, GO-N$_3$/PBIA-CN fibers with excellent impregnated performances show a broad prospect for applications in aeronautical engineering, special protection equipment, and civil fields (Figure S31, Supporting Information).

3. Conclusion

In summary, we reported a strategy to prepare high-mechanical-performance HAFs (GO-N$_3$/PBIA-CN) with a high IFSS of 40.04 ± 2.4 MPa and a high tensile strength of 5.08 ± 0.24 GPa. Mechanism analyses demonstrate that the design of chemical bonding between PBIA-CN chains and GO-N$_3$ in GO-N$_3$/PBIA-CN fibers can improve the interchain interaction to conquer the splitting of nanofibrils and strengthen the skin-core layer of fibers. GO-N$_3$ can improve the crystallinity and orientation degree of fibers by inducing a more ordered arrangement of PBIA-CN polymer chains. These two effects account for the simultaneous improvement in IFSS and tensile strength of GO-N$_3$/PBIA-CN fibers. Our work provides an effective strategy to prepare fiber materials with high interfacial and tensile properties.
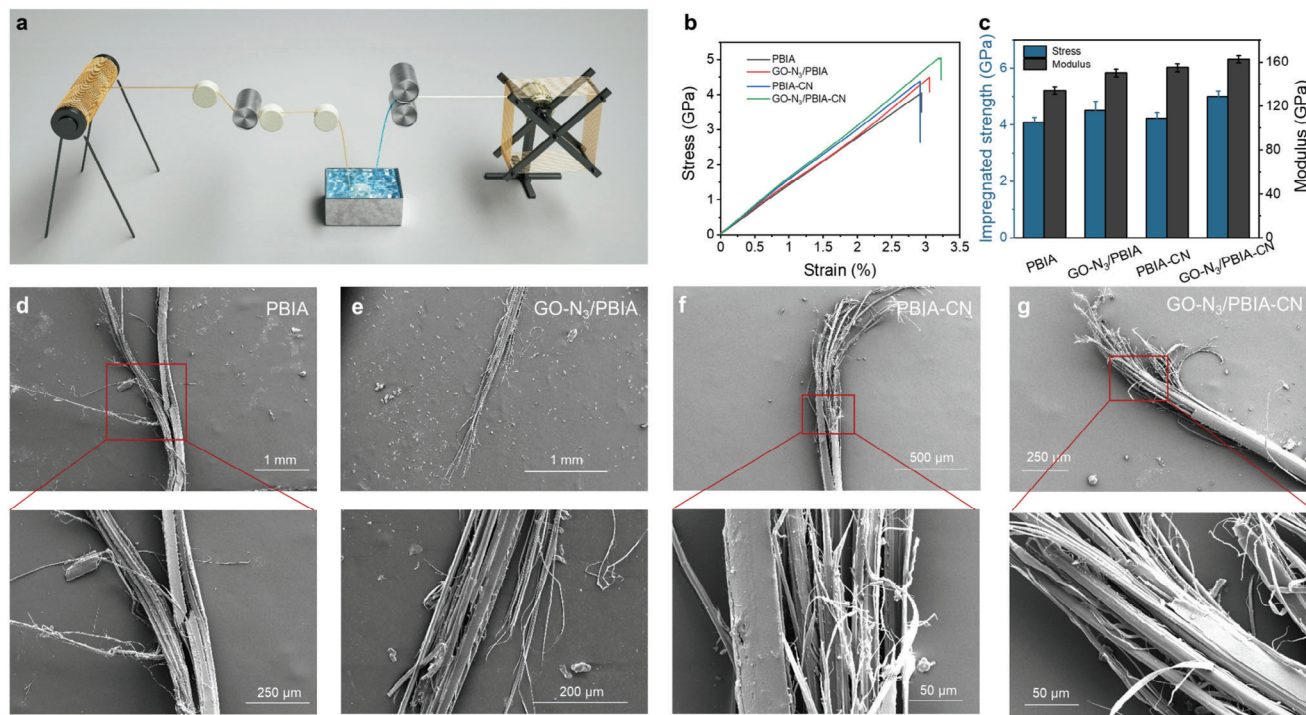
Figure 5. a) Schematic diagram of an impregnated process of fibers. b) Stress-versus-strain curves of different impregnated fibers. c) Comparison of the impregnated strength and modulus of different impregnated fibers. SEM images of the fracture point of impregnated d) PBIA, e) GO-N$_3$/PBIA, f) PBIA-CN, and g) GO-N$_3$/PBIA-CN fibers.

4. Experimental Section

Preparation of GO: GO was prepared by oxidation of the natural graphite powder according to a modified Hummers' method. Briefly, graphite (3 g) was added to the concentrated sulfuric acid (70 mL) and the mixture was vigorously stirred for 30 min at room temperature. Then, potassium permanganate (9 g) was added slowly to the reaction system to avoid increasing the temperature of the mixture. The first oxidation process was performed over 1 h under 35 °C, then 100 mL deionized water was added into the mixture to initiate the second oxidation process, and the mixture was kept at 95 °C for 15 min. The reaction was terminated by pouring the resultant slurry into icy deionized water and hydrogen peroxide (10 mL) was added into the dispersion. Next, the as prepared sample was washed with 2000 mL 1:10 v/v% HCl solution and deionized water by filtration. After that, GO was redispersed in deionized water and exfoliated by mild sonication at 20 °C for 20 min, and further purified by dialysis for 2 weeks. The resultant dispersion was centrifuged at 1000 g for 20 min to remove the unexfoliated graphite oxide. Finally, the dilute GO dispersion was concentrated by centrifugation at 10 000 g for 1 h to obtain high-concentrated GO dispersion (6 wt.%).

Preparation of GO-N$_3$: GO powder was dispersed in 4-morpholineethanesulfonic acid (MES) buffer (pH 6, 2 mg mL^{-1}). Then, 1-ethyl-3-(3-dimethylaminopropyl)carbodiimide (250 mg) and N-hydroxy succinimide (200 mg) were added to the solution, respectively. The dispersion was stirred for 30 min at room temperature. After that, N$_3$-PEG-NH$_3$ (PEG: polyethylene glycol, its molecular weight is 1000) was added and the reaction was kept for 12 h under stirring at room temperature. Then, the as-prepared GO-N$_3$ solution was purified by centrifuging and washed with deionized water. Finally, the GO-N$_3$ solution was treated by a freeze dryer to obtain GO-N$_3$ powder.

In Situ Synthesis of GO-N$_3$/PBIA-CN Spinning Dope: GO-N$_3$ powder (100 mg) was dispersed in dimethylacetamide (DMAc) using an Ultrasonic Cell Disruption System with 60% power (900 W) for 10 min in an ice bath under N$_2$ flow. The PPD, PPD-CN, and PABZ ((n_{PPD} + n_{PPD-CN}):n_{PABZ}

= 2:3; n_{PPD}:n_{PPD-CN} = 2:1) were added into the mixture containing LiCl and DMAc. Subsequently, the homogenous GO-N$_3$ dispersion was slowly added into the solution and the mixture was kept stirring for 1 h. After cooling the mixture to below 10 °C, the TPC was added into the reaction system several times, and then the reaction was conducted under stirring for 2 h. After the reaction, a black viscous spinning dope with a dynamic viscosity of 40 000—60 000 mPa s was obtained. As a control sample, the PBIA-CN spinning dope was obtained following a similar procedure without adding the GO-N$_3$ powder. The PBIA spinning dope was obtained following a similar preparation procedure without adding the PPD-CN monomer and the GO-N$_3$ powder. The GO-N$_3$/PBIA spinning dope was obtained following a similar preparation procedure without adding the PPD-CN monomer.

Fabrication of GO-N$_3$/PBIA-CN Fibers Through Wet-Spinning: The obtained GO-N$_3$/PBIA-CN spinning dope was first degassed in a vacuum, and then poured into a spinning pot on the spinning line. Under the extrusion by a spinning pump, the spinning dope was transported to a spinneret plate, and injected into a primary coagulation bath consisting of 50% DMAc and 50% distilled water with an injection speed of 3 m min^{-1}. The as-coagulated gel fibers were drawn with a rate of 2 m min^{-1} in the primary coagulation bath. The size of the spinneret hole is 100 μm. The gel fibers then were drawn in a secondary coagulation bath consisting of 20% DMAc and 80% distilled water with a draw ratio of 2. The draw rate is 4 m min^{-1}. The primary fiber was obtained after the washing and drying process (120 °C). Subsequently, the GO-N$_3$/PBIA-CN fibers were obtained after a heating treatment (390 °C) in the N$_2$ atmosphere and collected via an automatic winding device. The PBIA fibers, GO-N$_3$/PBIA fibers, and PBIA-CN fibers were prepared under the same procedures by adding corresponding spinning dopes.

Calculation on the Binding Energy: The binding energy was obtained from density functional theory-based tight-binding (DFTB) calculations, which were carried out using the DFTB+ package.[61] All DFTB computations were performed with DFT-D3 dispersion correction with Becke–Jonhson damping.[62,63] The 3-ob-1 Slater-Koster set of parameters was employed.[64–66] Energy-minimized optimization tests were conducted

**ADVANCED
SCIENCE NEWS**

www.advancedsciencenews.com

**ADVANCED
FUNCTIONAL
MATERIALS**

www.afm-journal.de

using a conjugate gradient algorithm with a force-threshold criterion of 10^{-6} Hartree/Bohr. The hybrid systems of PBIA/PBIA, PBIA-CN/PBIA-CN, PBIA/epoxy, PBIA-CN/epoxy, and GO/PBIA-CN were established and optimized. The aperiodic boundary conditions were adopted along all directions for all systems, except for in-plane directions of GO/PBIA-CN, and the thickness of the vacuum layer was over 3 nm along the aperiodic directions. Finally, the binding energy was calculated as follows:

$$E_b = (E_a + E_b - E_{total}) / n \qquad (1)$$

where E_a and E_b are the energy of the isolated polymer chain (GO sheet), E_{total} is the total energy of the composite system, and n is the total number of atoms in the composite system.

IFSS Measurement Method at High Loading Rates: The IFSS between the fibers and the matrix under dynamic loading is measured by a mini-split Hopkinson tension bar (mini-SHTB) as illustrated in Figure S21 (Supporting Information). As the sleeve-type bullet launched by the gas gun impacts the mass block fixed at the end of the incident bar, a tensile wave is generated and propagates along the incident bar toward the specimen. Once it reaches the microdroplet specimen clamped at the other end of the incident bar, the dynamic shear is applied to the interface between the fiber and the microdroplet matrix, leading to its ultimate failure. A quartz piezoelectric force sensor with ultrahigh-frequency response (Kistler 9001, 180 kHz) is utilized to measure directly the shear force applied on the interface. The IFSS can therefore be analyzed based on the failure load and the interface area,

$$\tau = \frac{F}{\pi d_f l_e} \qquad (2)$$

where τ represents IFSS, F is the failure load when the interface debonds. d_f and l_e are the diameter of the fiber and its embedded length in the microdroplet, respectively.

Characterizations: The detailed morphology and structure of GO-N$_3$ and fibers were investigated by SEM (FEI Quattro S, acceleration voltage 5–10 kV, the fiber samples were treated with gold spraying for 180 s before observation), optical microscope (LV100ND, Nikon, Japan), XPS (Kratos Analytical Axis-Ultra spectrometer with Al Kα X-ray source), atomic force microscope (AFM; Bruker Dimension Icon), and Fourier transform infrared spectroscopy (FT-IR; IRTracer-100, Shimadzu, Japan). The cross-section of GO-N$_3$/PBIA-CN fiber was cut by Ultramicrotome (Leica EM UC6). The observation of GO-N$_3$ inside fibers was operated by TEM (FEI Tecnai F20, acceleration voltage 200 kV).

Supporting Information

Supporting Information is available from the Wiley Online Library or from the author.

Acknowledgements

Conflict of Interest

The authors declare no conflict of interest.

Author Contributions

J.L. and Y.W. contributed equally to this work. J.Z. and K.J. conceived and supervised the project. J.L. and Y.W. performed the preparation of fibers, with assistance from T.L., Z.Z., Z.X., and Z.G. X.J. performed the theoretical calculations and simulations, with assistance from E.G. X.L. performed dynamic mechanical tests, with assistance from X.W. All authors contributed to discussions and commented on the manuscript.

Data Availability Statement

The data that support the findings of this study are available from the corresponding author upon reasonable request.

Keywords

[1] F. Chen, L. Zhai, H. Yang, S. Zhao, Z. Wang, C. Gao, J. Zhou, X. Liu, Z. Yu, Y. Qin, W. Xu, *Adv. Sci.* **2021**, *8*, 2004171.

[2] H. Wang, H. Wang, Y. Wang, X. Su, C. Wang, M. Zhang, M. Jian, K. Xia, X. Liang, H. Lu, S. Li, Y. Zhang, *ACS Nano* **2020**, *14*, 3219.

[3] I. Azpitarte, A. Zuzuarregui, H. Ablat, L. Ruiz-Rubio, A. López-Ortega, S. D. Elliott, M. Knez, *Chem. Mater.* **2017**, *29*, 10068.

[4] H. Cai, D. Shen, L. Yuan, Q. Guan, A. Gu, G. Liang, *Appl. Surf. Sci.* **2018**, *452*, 389.

[5] M. M. Houck, in *Identification of Textile Fibers*, Woodhead Publishing, Cambridge **2009**, p. 88.

[6] M. Afshari, D. J. Sikkema, K. Lee, M. Bogle, *Polym. Rev.* **2008**, *48*, 230.

[7] R. Kotek, D. Jung, A. E. Tonelli, N. Vasanthan, *J. Macromol. Sci. C* **2005**, *45*, 201.

[8] M. Afshari, A. Gupta, D. Jung, R. Kotek, A. E. Tonelli, N. Vasanthan, *Polymer* **2008**, *49*, 1297.

[9] J. W. Downing, J. A. Newell, *J. Appl. Polym. Sci.* **2004**, *91*, 417.

[10] S.-H. Zhang, G.-Q. He, G.-Z. Liang, H. Cui, W. Zhang, B. Wang, *Appl. Surf. Sci.* **2010**, *256*, 2104.

[11] J. Li, Y. Wen, Z. Xiao, S. Wang, L. Zhong, T. Li, K. Jiao, L. Li, J. Luo, Z. Gao, S. Li, Z. Zhang, J. Zhang, *Adv. Funct. Mater.* **2022**, *32*, 2200937.

[12] J. Luo, Y. Wen, X. Jia, X. Lei, Z. Gao, M. Jian, Z. Xiao, L. Li, J. Zhang, T. Li, H. Dong, X. Wu, E. Gao, K. Jiao, J. Zhang, *Nat. Commun.* **2023**, *14*, 3019.

[13] Z. Zhang, X. Jia, C. Li, L. Li, Y. Wen, Z. Gao, J. Zhang, E. Gao, K. Jiao, J. Zhang, *Nano Res.* **2023**, *16*, 12286.

[14] K. Li, L. Luo, J. Huang, H. Wang, Y. Feng, X. Liu, *J. Appl. Polym. Sci.* **2015**, *132*, 42482.

[15] X. Ding, H. Kong, M. Qiao, Z. Hu, M. Yu, *Polymers* **2019**, *11*, 856.

[16] H. G. Chae, S. Kumar, *Science* **2008**, *319*, 908.

[17] J. H. Park, G. C. Rutledge, *Macromolecules* **2017**, *50*, 5627.

[18] S. Sockalingam, R. Bremble, J. W. Gillespie, M. Keefe, *Compos. Part. A Appl. Sci. Manuf.* **2016**, *81*, 271.

[19] Y. Dai, Y. Han, Y. Yuan, C. Meng, Z. Cheng, L. Luo, J. Qin, X. Liu, *Macromol. Mater. Eng.* **2018**, *303*, 1800076.

**ADVANCED
SCIENCE NEWS**

www.advancedsciencenews.com

**ADVANCED
FUNCTIONAL
MATERIALS**

www.afm-journal.de

[20] Z. Cheng, L. Zhang, C. Jiang, Y. Dai, C. Meng, L. Luo, X. Liu, *Chem. Eng. J.* **2018**, *347*, 483.

[21] T. A. Stockdale, D. P. Cole, J. M. Staniszewski, M. R. Roenbeck, D. Papkov, S. R. Lustig, Y. A. Dzenis, K. E. Strawhecker, *ACS Appl. Mater. Interfaces* **2020**, *12*, 22256.

[22] B. Larin, C. A. Avila-Orta, R. H. Somani, B. S. Hsiao, G. Marom, *Polymer* **2008**, *49*, 295.

[23] J. M. García, F. C. García, F. Serna, J. L. De La Peña, *Prog. Polym. Sci.* **2010**, *35*, 623.

[24] Y. Rao, A. J. Waddon, R. J. Farris, *Polymer* **2001**, *42*, 5937.

[25] R. J. Young, D. Lu, R. J. Day, W. F. Knoff, H. A. Davis, *J. Mater. Sci.* **1992**, *27*, 5431.

[26] A. A. Leal, J. M. Deitzel, J. W. Gillespie Jr, *Compos. Sci. Technol.* **2007**, *67*, 2786.

[27] A. A. Leal, J. M. Deitzel, J. W. Gillespie Jr, *J. Compos. Mater.* **2009**, *43*, 661.

[28] A. Knijnenberg, J. Bos, T. J. Dingemans, *Polymer* **2010**, *51*, 1887.

[29] J. Wollbrett-Blitz, S. Joannès, R. Bruant, C. Le Clerc, M. Romero De La Osa, A. Bunsell, A. Marcellan, *J. Polym. Sci. B Polym. Phys.* **2016**, *54*, 374.

[30] H. Ge, H. Liu, J. Chen, C. Wang, *J. Appl. Polym. Sci.* **2008**, *108*, 947.

[31] K. Sahin, J. K. Clawson, J. Singletary, S. Horner, J. Zheng, A. Pelegri, I. Chasiotis, *Polymer* **2018**, *140*, 96.

[32] A. A. Leal, J. M. Deitzel, S. H. Mcknight, J. W. Gillespie Jr, *Polymer* **2009**, *50*, 1228.

[33] L. Luo, Y. Wang, Y. Dai, Y. Yuan, C. Meng, Z. Cheng, X. Wang, X. Liu, *J. Mater. Sci.* **2018**, *53*, 13291.

[34] Y. H. Zhang, Y. D. Huang, L. Liu, K. L. Cai, *Appl. Surf. Sci.* **2008**, *254*, 3153.

[35] Y. Yang, C. Min, Z. Xu, H. Liang, Q. Li, M. Ji, S. Liu, W. Wang, N. Li, X. Pei, *Mater. Today Chem.* **2022**, *24*, 100795.

[36] X. Gong, Y. Liu, M. Huang, Q. Dong, N. Naik, Z. Guo, *Compos. Commun.* **2022**, *29*, 100996.

[37] L. X. Xing, L. Liu, M. He, Z. J. Wu, Y. D. Huang, *Adv. Mater. Res.* **2013**, *658*, 80.

[38] B. A. Patterson, H. A. Sodano, *ACS Appl. Mater. Interfaces* **2016**, *8*, 33963.

[39] J. Nasser, J. Lin, K. Steinke, H. A. Sodano, *Compos. Sci. Technol.* **2019**, *174*, 125.

[40] D. Chakraborty, S. Saha, S. Dey, S. Pramanik, *J. Appl. Polym. Sci.* **2020**, *137*, 48802.

[41] Z. Cheng, C. Chen, J. Huang, T. Chen, Y. Liu, X. Liu, *Appl. Surf. Sci.* **2017**, *401*, 323.

[42] Z. Cheng, Y. Liu, C. Meng, Y. Dai, L. Luo, X. Liu, *Compos. Sci. Technol.* **2019**, *182*, 107721.

[43] F. Xie, L. Xing, L. Liu, Y. Liu, H. Xu, Z. Zhong, C. Jia, Y. Huang, *Polym. Compos.* **2018**, *39*, E2436.

[44] L. Zhang, H. Kong, M. Qiao, X. Ding, M. Yu, *Polymers* **2019**, *11*, 1397.

[45] J. Lv, Z. Cheng, H. Wu, T. He, J. Qin, X. Liu, *Compos. Part B: Eng.* **2020**, *182*, 107608.

[46] I. A. Kinloch, J. Suhr, J. Lou, R. J. Young, P. M. Ajayan, *Science* **2018**, *362*, 547.

[47] X. Sun, H. Sun, H. Li, H. Peng, *Adv. Mater.* **2013**, *25*, 5153.

[48] D. G. Papageorgiou, Z. Li, M. Liu, I. A. Kinloch, R. J. Young, *Nanoscale* **2020**, *12*, 2228.

[49] Y. Wen, M. Jian, J. Huang, J. Luo, L. Qian, J. Zhang, *Nano Lett.* **2022**, *22*, 6035.

[50] J. N. Coleman, U. Khan, W. J. Blau, Y. K. Gun'ko, *Carbon* **2006**, *44*, 1624.

[51] V. D. Punetha, S. Rana, H. J. Yoo, A. Chaurasia, J. T. Mcleskey, M. S. Ramasamy, N. G. Sahoo, J. W. Cho, *Prog. Polym. Sci.* **2017**, *67*, 1.

[52] Y. Liu, S. Kumar, *ACS Appl. Mater. Interface* **2014**, *6*, 6069.

[53] Z. Gao, J. Zhu, S. Rajabpour, K. Joshi, M. Kowalik, B. Croom, Y. Schwab, L. Zhang, C. Bumgardner, K. R. Brown, D. Burden, J. W. Klett, A. C. T. Van Duin, L. V. Zhigilei, X. Li, *Sci. Adv.* **2020**, *6*, eaaz4191.

[54] J. Luo, L. Yang, D. Sun, Z. Gao, K. Jiao, J. Zhang, *Small* **2020**, *16*, 2003426.

[55] T. Li, Z. Meng, S. Keten, *Carbon* **2020**, *158*, 303.

[56] T. Ramanathan, A. A. Abdala, S. Stankovich, D. A. Dikin, M. Herrera-Alonso, R. D. Piner, D. H. Adamson, H. C. Schniepp, X. Chen, R. S. Ruoff, S. T. Nguyen, I. A. Aksay, R. K. Prud'homme, L. C. Brinson, *Nat. Nanotechnol.* **2008**, *3*, 327.

[57] X. Ming, A. Wei, Y. Liu, L. Peng, P. Li, J. Wang, S. Liu, W. Fang, Z. Wang, H. Peng, J. Lin, H. Huang, Z. Han, S. Luo, M. Cao, B. Wang, Z. Liu, F. Guo, Z. Xu, C. Gao, *Adv. Mater.* **2022**, *34*, 2201867.

[58] B. Qiu, T. Sun, M. Yuan, H. Zhang, Y. Chen, S. Zhou, Z. Heng, M. Liang, H. Zou, *Compos. Sci. Technol.* **2021**, *213*, 108939.

[59] P. Sundberg, R. Larsson, B. Folkesson, *J. Electron Spectrosc. Relat. Phenom.* **1988**, *46*, 19.

[60] Y. Wang, G. Liu, G. Peng, S. Li, F. Xie, *J. Mater. Eng.* **2018**, *46*, 140.

[61] B. Hourahine, B. Aradi, V. Blum, F. Bonafé, A. Buccheri, C. Camacho, C. Cevallos, M. Y. Deshaye, T. Dumitrica, A. Dominguez, S. Ehlert, M. Elstner, T. Van Der Heide, J. Hermann, S. Irle, J. J. Kranz, C. Köhler, T. Kowalczyk, T. Kubar, I. S. Lee, V. Lutsker, R. J. Maurer, S. K. Min, I. Mitchell, C. Negre, T. A. Niehaus, A. M. N. Niklasson, A. J. Page, A. Pecchia, G. Penazzi, et al., *J. Chem. Phys.* **2020**, *152*, 124101.

[62] S. Grimme, J. Antony, S. Ehrlich, H. Krieg, *J. Chem. Phys.* **2010**, *132*, 154104.

[63] S. Grimme, S. Ehrlich, L. Goerigk, *J. Comput. Chem.* **2011**, *32*, 1456.

[64] M. Gaus, A. Goez, M. Elstner, *J. Chem. Theory Comput.* **2013**, *9*, 338.

[65] M. Gaus, X. Lu, M. Elstner, Q. Cui, *J. Chem. Theory Comput.* **2014**, *10*, 1518.

[66] X. Lu, M. Gaus, M. Elstner, Q. Cui, *J. Phys. Chem. B* **2015**, *119*, 1062.

2310008 (10 of 10)